Supplementary Information

Guangzong Xiao[1,3,7,*], Zijian Feng[1,3,7], Tengfang Kuang[1,3], Ran Huang[5], Yutong He[1,3], Xinlin Chen[1,3], Yunlan Zuo[2], Xiang Han[1,3], Wei Xiong[1,3], Zhongqi Tan[1,3], Adarsh Ganesan[4], Franco Nori[5], Cheng-Wei Qiu[6], Hui Luo[1,3,*], Hui Jing[2,*]

[1]College of Advanced Interdisciplinary Studies, NUDT, Changsha, China

[2]Department of Physics, Hunan Normal University, Changsha, China

[3]Nanhu Laser Laboratory, NUDT, Changsha, China

[4]School of Engineering and Applied Sciences, Ahmedabad University, India

[5]Quantum Computing Center and Cluster for Pioneering Research, RIKEN, Saitama, Japan

[6]Department of Electrical & Computer Engineering, National University of Singapore, Singapore

[7]These authors contributed equally to this work

*xiaoguangzong@nudt.edu.cn; luohui.luo@163.com; jinghui@hunnu.edu.cn.

1. EXPERIMENTAL DETAILS

1.1 SCHEME FOR THE DISPLACEMENT MEASUREMENT

By utilizing a Laser Doppler Velocimetry (LDV), we can acquire precise membrane displacement signals. Limited by the bandwidth and resolution of the LDV, we propose a novel approach to measure the amplitude of the membrane, as illustrated in Fig. S1.1. The laser reflected from the membrane is directed onto the D-shaped mirror through the beam splitter mirror. The beam is then split into two parts for differential detection using a balanced photodetector with a broader bandwidth. The vibration of the membrane causes a geometrical deflection of the beam, as described in the Section 2.1. According to the simulation results, membrane deformation is linearly coupled with beam deflection. Therefore, it can be assumed that the membrane displacement is linear with the change in optical power under very small displacements.

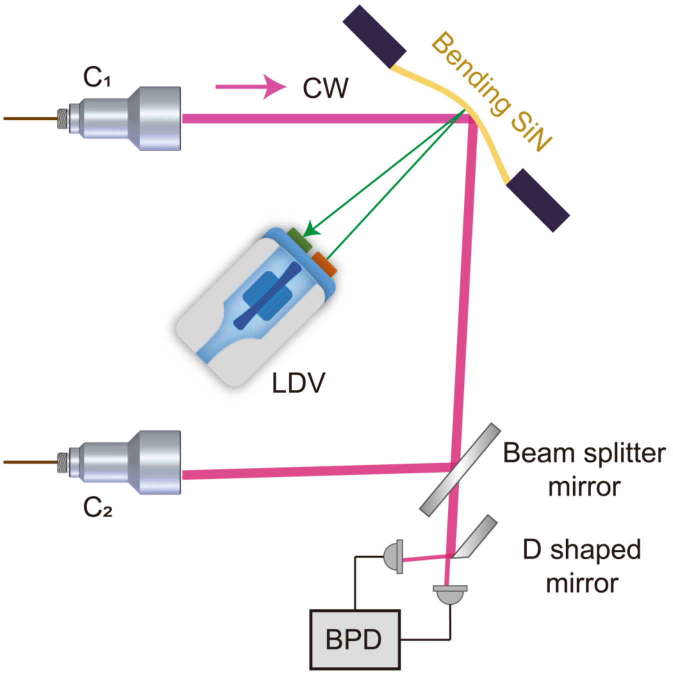

Figure S1.1. Scheme for the displacement measurement. CW, clockwise; LDV, Laser Doppler Velocimeter; BPD, balanced photodetector.

In the experiment, we apply both LDV and differential detection for displacement measurement. The accurate data from the LDV is used to calibrate the optical power signal obtained from the differential detection, which in turn provides the displacement signal of the membrane. Afterwards, the displacement signals are fed into the spectrum analyser.

1.2 FREQUENCY SPECTRUM OF THE COHERENT AFC

By adjusting the pumping power and the deflection angle of the mirror M, it is possible to regulate the number of comb teeth and the teeth spacing of the phonon laser frequency comb. In our system, the phonon lasers inherently have multiple harmonics, which are caused by optomechanical coupling nonlinearity. By gradually increasing the pumping power and adjusting the mirror angle to prevent mechanical wave mixing, an increase in the number of harmonics can be observed. We have realised nonlinear phonon lasers with up to 200 harmonics, as illustrated in Fig. S1.2, which has never been reported in our prior research or in other phonon laser systems. The teeth spacing remains at 125 kHz, which corresponds to the fundamental mode frequency of the membrane vibration. Multi-frequency phonon lasers reach a bandwidth of approximately 28 MHz. Due to the strong pumping power, which can increase the intensity of the phonon laser, the generation of mechanical wave mixing is inevitable, especially noticeable in the low-frequency region.

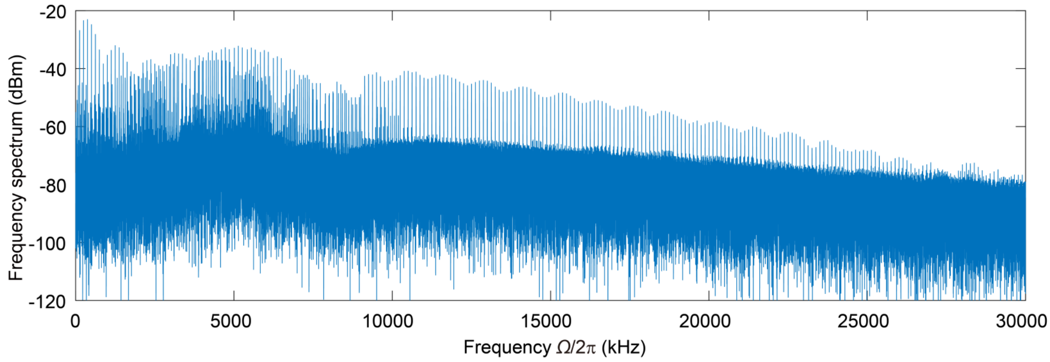

Figure S1.2. Frequency spectrum of multi-frequency phonon lasers. The teeth spacing is about 125kHz, the fundamental mode frequency of the membrane. The number of nonlinear harmonics is more than 200.

Based on the phonon laser, we first introduce the mechanical wave mixing mechanism and realise the phonon laser frequency combs with up to 10^4 comb teeth, as shown in Fig. S1.3. This peak has never been reached by other acoustic frequency combs (AFC). The spacing of this frequency comb is about 1 kHz, as can be seen in the insets. In this case, the phonon laser frequency combs are weakened and drowned out by noise when the bandwidth exceeds 12 MHz. The bandwidth of the phonon laser comb with mechanical wave mixing is smaller than that of the multi-frequency phonon lasers, because some of the energy is utilized in the mechanical wave mixing process, leading to a more pronounced attenuation in the high-frequency range. At the same time, the large number of comb teeth leads to an inevitable weakening in some of the sidebands generated by multiple mechanical wave mixings.

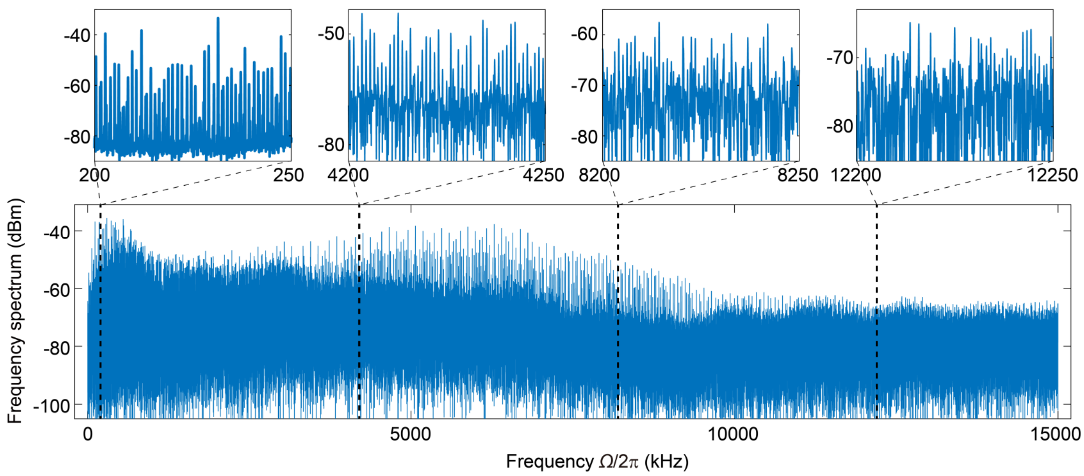

Figure S1.3. Frequency spectrum of the coherent acoustic frequency comb. The teeth spacing is about 1kHz and the bandwidth is about 12Mhz. Thus, the teeth number is up to 10^4.

1.3 TIME DOMAIN OF THE COHERENT AFC

In the experiment, we utilized the LDV to record the growth of the phonon laser frequency comb, as shown in Fig. S1.4. It can be seen that the membrane experiences growth of about 1 second after turning on the pumping laser. Moreover, the membrane amplitude decreases slightly after reaching the maximum and enters a steady phonon-lasing regime. Compared with the other AFC in the optomechanical system [S1], our growth period (1 s) is shorter than that of overtone frequency combs (24 s).

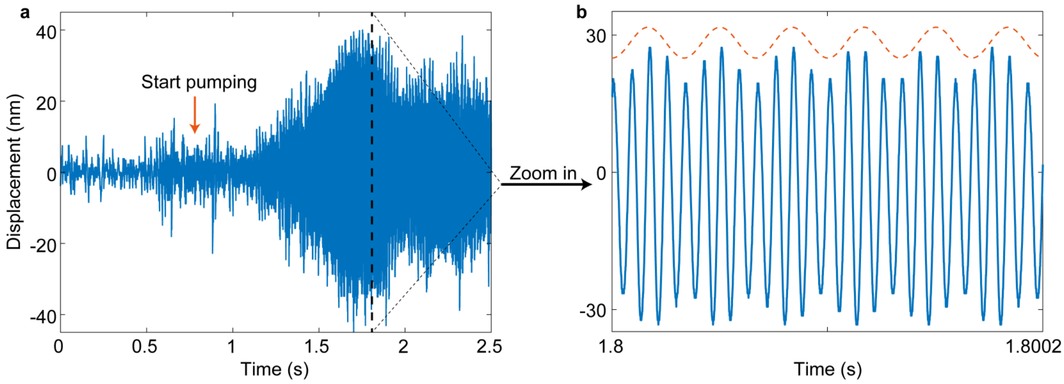

Figure S1.4. Time-domain frequency combs. a. Measured displacement of the membrane, showing clear growth before reaching a plateau around 1 s. **b.** Zoom-in of time-domain signal in **a**.

1.4 ACOUSTIC FREQUENCY COMBS IN VARIOUS SYSTEMS

Table 1 displays the acoustic frequency combs in various systems. AFCs have been implemented in electromechanical systems [S2-S6], opto-electromechanical systems [S7, S8], and optomechanical systems [S1] in recent years. Although acoustic frequency combs have been realised in various systems, phonon lasing has never been reported or demonstrated. These incoherent acoustic frequency combs are difficult to apply in practice.

In contrast, our system generates acoustic frequency combs based on the multi-frequency phonon lasers, which are inherently coherent. Moreover, in comparison to the electro-mechanical and opto-electro-mechanical systems, our frequency comb is driven by the intracavity optical field without the need for a driving signal with a similar frequency to the oscillator. In addition, we can enhance the number of comb teeth by up to two orders of magnitude. New comb teeth generated from cascaded four-wave mixing are steered for each phonon lasing mode, leading to a significant increase in the number of comb teeth. Acoustic frequency combs with numerous comb teeth are highly advantageous in practical applications, such as precision measurements.

Furthermore, the frequency range of this work is from 13 Hz to 28 MHz, extending the acoustic frequency combs from ultrasound to audible sound and even infrasound for the first time. Thus, our coherent AFC have broader application scenarios.

Table S1 | Comparison of acoustic frequency combs

Type	System	Mechanism of combs	Phonon lasing	Teeth spacing	Number of comb teeth	Magnitude of the frequency range
Electro-mechanics	Micro-cantilever[S2]	Wave mixing	×	0.01 ~ 10 Hz	~ 100	280 kHz
	Nano-strings[S3]	Wave mixing	×	1 ~ 10 kHz	~ 10	6.6 MHz
	Free-beam[S4]	Wave mixing	×	2 ~ 10 kHz	~ 20	3.8 MHz
	Coupled cantilevers[S5]	Bifurcation	×	0.5 ~ 5 Hz	~ 25	155 kHz
	Bulk acoustic[S6]	Bifurcation	×	0.7 ~ 2 Hz	~ 30	5.5 MHz
Opto-electro-mechanics	MoS_2 monolayer[S7]	Bifurcation	×	200 ~ 700 kHz	~ 100	10 MHz
	Graphene[S8]	Bifurcation	×	110 ~ 440 kHz	~ 10	22 ~ 44 MHz
Opto-mechanics	Trampoline membrane[S1]	Overtone-nonlinearity	×	120 ~ 360 kHz	~ 35	100 kHz ~ 4 MHz
	This work	Optomechanical nonlinearity	✓	10Hz ~ 100kHz	~ 10^4	13 Hz ~ 28 MHz

Notation: ✓ for Yes; × for No.

2. THEORY

2.1 DISSIPATIVE COUPLING BETWEEN MEMBRANE AND LASER

Figure S2.1 illustrates the dissipative coupling between membrane deformation and intracavity laser in the active cavity optomechanical system. The membrane deforms under the optical force, causing the reflected light to be deflected. Thus, the bending SiN membrane in the ring cavity results in the geometrically deflecting loss. The optical forces exerted on the surface of the membrane are consequently weakened, causing the membrane's deformation to decrease conversely.

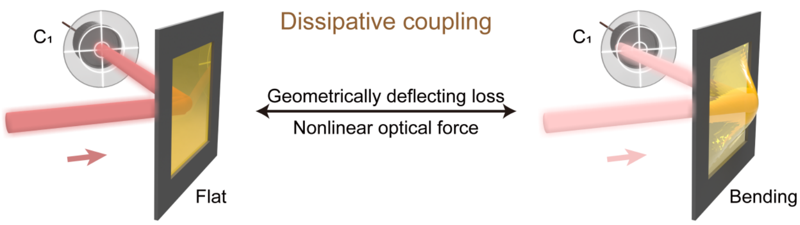

Figure S2.1. Schematic of the dissipative coupling. The membrane deforms, in the presence of optical forces, however, causing an increase in geometrically deflecting loss. In turn, the intracavity power is reduced and the membrane's deformation decreases

We have specifically investigated the relationship between the membrane deformation and the geometric deflection of the beam to study the dissipative coupling between the membrane and the intracavity laser in depth. For simplicity, we only consider the vibration in the fundamental mode of the membrane and regard the membrane as an arc with the radius of curvature R.

The angle between the incident light and the initial membrane plane is set to be φ, the beam diameter is D, the membrane length is L, the displacement of the membrane is x, α, β, γ represent the angles of the incident rays, θ is the divergence angle of the reflected beam, $\Delta\theta$ is the deflection angle of the reflected beam. The detailed geometrical relationship is shown in Fig. S2.1, where the relationship between the radius of curvature R and the displacement x satisfies $R^2 = (L/2)^2 + (R-x)^2$. Fig. S2.2a shows a schematic diagram of a light beam with a diameter D incident on the membrane, emphasizing the convergence of the reflected beam. Fig. S2.2b is a schematic diagram of a ray incident on the centre of the membrane, primarily investigating the transverse deflection of the reflected ray and the change in the reflecting angle.

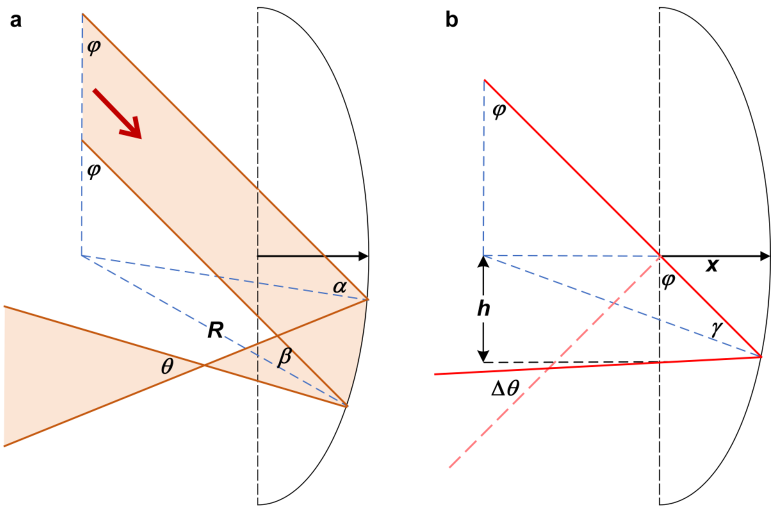

Figure S2.2. Geometric deflection caused by the bending membrane. a. The schematic of a beam with a diameter D incident on the membrane. **b.** The schematic of a ray incident on the centre of the membrane.

Assuming that the optical axis is incident on the centre of mass of the original membrane, the sines of the three incident angles α, β, γ can be obtained according to the sine theorem.

$$\sin\alpha = \frac{R-x}{R}\cos\varphi + D/2R$$
$$\sin\beta = \frac{R-x}{R}\cos\varphi - D/2R \quad (1)$$
$$\sin\gamma = \frac{R-x}{R}\cos\varphi$$

Based on the geometric relationship, the divergence angle of the reflected beam θ is

$$\begin{aligned}\theta &= 2\alpha - 2\beta \\ &= 2\sin^{-1}\left(\frac{R-x}{R}\cos\varphi + D/2R\right) \\ &\quad -2\sin^{-1}\left(\frac{R-x}{R}\cos\varphi - D/2R\right)\end{aligned} \quad (2)$$

Setting the range of membrane deformation as 0-10 nm, the angle between the incident light and the membrane as φ = 45°, the simulation results illustrating the relationship between the divergence angle θ and the membrane displacement x are presented in Fig. S2.3a.

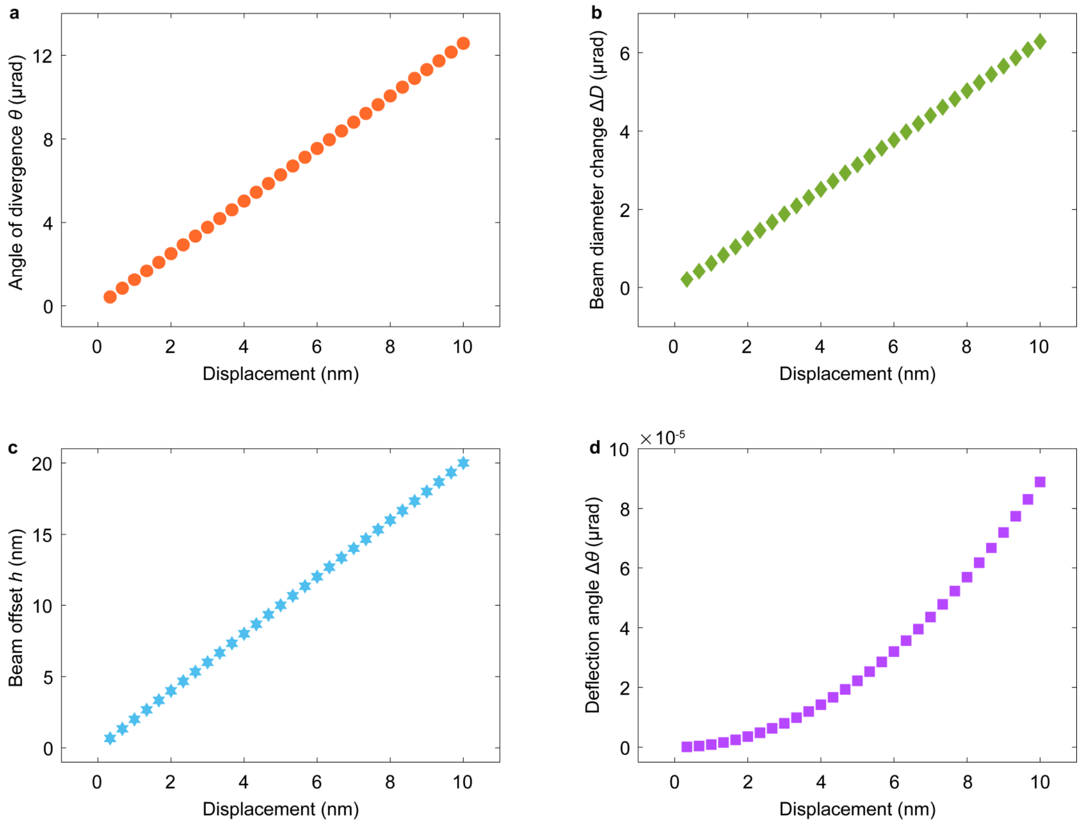

Figure S2.3. Simulation results of the geometric deflection caused by the bending membrane. **a.** Angle of divergence θ, **b.** Beam diameter change ΔD, **c.** Beam offset h, **d.** Deflection angle $\Delta\theta$, versus the membrane's displacement.

Further, the change in beam diameter when the beam propagates a distance of L_0 is $\Delta D = 2L_0 \tan\frac{\theta}{2}$. Assuming the propagation distance L_0 = 1 m, the simulation results are shown in Fig. S2.3b.

The deformation of the membrane can lead to a transverse deflection h of the beam, which is calculated as:

$$h = \frac{\sin 2\gamma}{\sin(2\gamma+\varphi)} \frac{\sin[(90+\varphi+\gamma)/2]}{\sin[(90+\varphi-\gamma)/2]} x \tag{3}$$

The simulation results are shown in Fig. S2.3c.

In addition, the membrane's deformation causes the reflection angle to deflect with an angle of $\Delta\theta = 90 - 2\gamma$, compared to the original reflected beam (see Fig. S2.3d).

The membrane's displacement will result in a geometrical deflection of the reflected light, leading to a decrease in the coupling efficiency of the spatial light at the collimator and, consequently, causing cavity loss. By employing the model that connects membrane displacement and the geometrical deflection of the reflected light, we can establish the relationship between the membrane displacement x and the geometrically deflecting loss δ_g, which in turn allows us to derive the expression for the intracavity power P [S9].

$$P(x) = P_0 \left[\frac{\mu P_{\text{pump}}}{\delta_{\text{i}} + \delta_{\text{g}}(x)} - 1 \right] \tag{4}$$

where P_0 is the proportion coefficient, μ is the gain factor, P_{pump} is the pumping power, and δ_{i} is the loss of the cavity itself.

The dissipative coupling strength can be calculated by experimentally measuring the change in intracavity laser power P with respect to the displacement x.

$$\frac{\partial\kappa}{\partial x} = \frac{c}{2\pi L} \cdot \frac{\partial\delta_{\text{g}}}{\partial x} = \frac{c}{2\pi L} \cdot \frac{\mu P_{\text{pump}} P_0}{(P+P_0)^2} \cdot \frac{\partial P}{\partial x} \tag{5}$$

In the experiment, we adjusted the ring cavity to minimize intracavity loss and maximize output power. When the mirror M is rotated under these conditions, it deflects the light, resulting in geometric deflection loss. The intracavity laser power is recorded as shown in Fig. S2.4a. The corresponding dissipative coupling strength is calculated in Fig. S2.4b using Eq. (5).

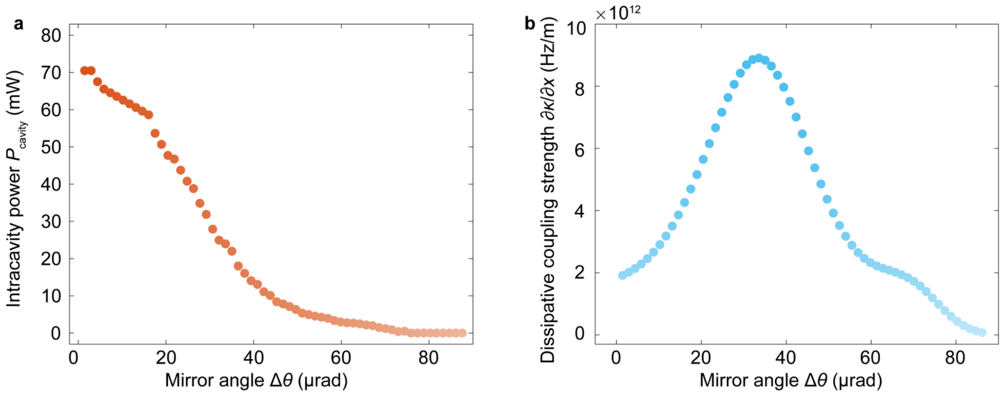

Figure S2.4. Intracavity laser power and dissipative coupling strength. a. The intracavity power P_{cavity} versus the mirror angle $\Delta\theta$. **b.** The dissipative coupling strength $\partial\kappa/\partial x$ as a function of the mirror angle $\Delta\theta$.

We note that this dissipative coupling mechanism will introduce significant optical loss, making it challenging to implement in previous optomechanical systems. A Yb^{3+}-doped gain fibre is applied to form an active cavity in our experimental system. The additional optical gain can effectively compensate for the geometrically deflecting loss, overcoming the contradiction in a dissipative system between strong dissipative coupling and strong laser output.

The dissipative coupling strength is an order of magnitude higher than that in our previous work, which accounts for the generation of high-quality multi-frequency phonon lasers with more harmonics.

2.2 RADIATION PRESSURE AND PHOTOTHERMAL PRESSURE

The temporal evolution of the SiN membrane can be described by Duffing equation[S10]

$$m\ddot{x} + m\gamma\dot{x} + m\Omega_0^2 x + m\beta x^3 = F_{\text{rp}}(x) + F_{\text{pth}}(x) + F_{\text{th}} \tag{6}$$

where m represents the effective mass of the membrane, x is the membrane's displacement, γ is the gas damping, Ω_0 is the natural frequency, β is the cubic nonlinearity coefficient from the membrane's mechanical nonlinearity, and F_{pth} is the thermal motion force. The optical force exerted on the membrane mainly consists of radiation pressure F_{rp} and photothermal pressure F_{pth}.

To determine the dominant force between radiation pressure and photothermal force, we analyse the direction of the frequency shift [S11] when increasing the pumping power, thereby strengthening both optical forces. It can be seen from Fig. S2.5 that there is a tendency for the resonant frequency to decrease with the gradual increase of the pumping power, indicating a more significant effect of the photothermal force.

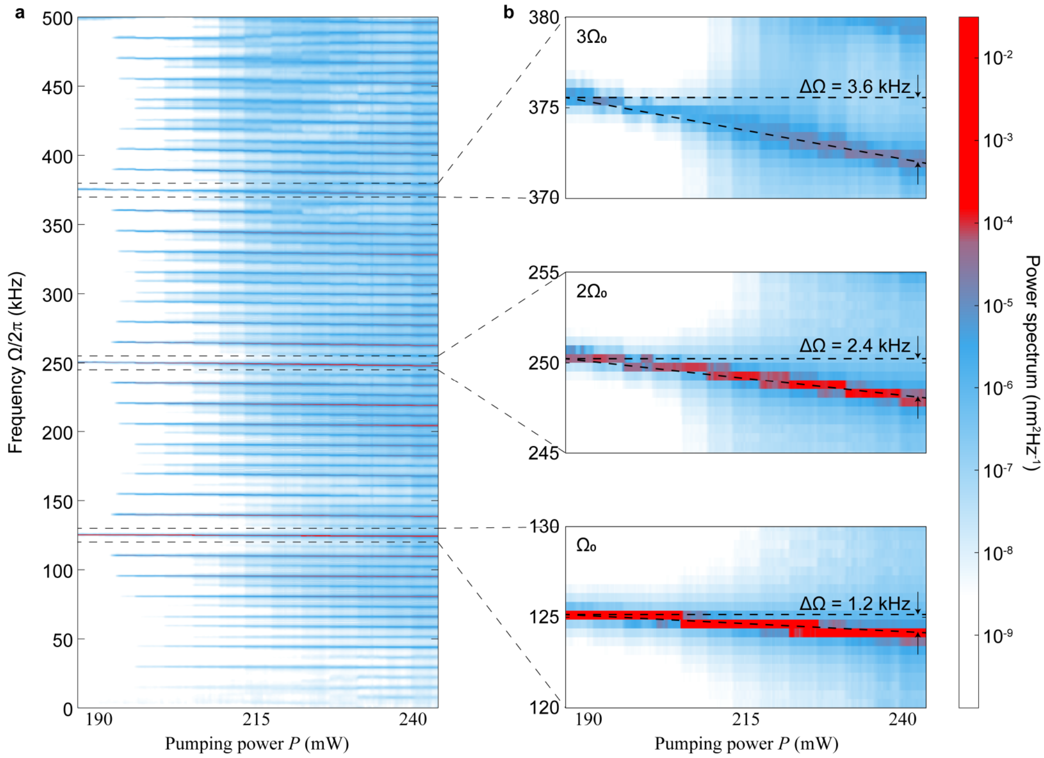

Figure S2.5. Intracavity laser power and dissipative coupling strength. a. Evolution of the power spectrum along with increased pumping power from 190 to 240 mW. **b.** Zoom-in of the power spectrum, indicating the frequency shifts of the fundamental mode Ω_0 and its harmonics $2\Omega_0$, $3\Omega_0$ with the increasing power.

2.3 MECHANICAL WAVE MIXING

The membrane is capable of producing four-wave mixing due to its inherent mechanical nonlinearity. Let us consider the membrane with cubic nonlinearity. Since both position x and resonance frequency Ω_0 depend on temperature T, we have

$$\ddot{x}+\gamma\left(\dot{x}-A\dot{T}\right)+\Omega_0^2\left(1+BT\right)\left(x-AT\right)+\beta\left(x-AT\right)^3=F_{\text{opt}}\left(x,t\right) \tag{7}$$

where A and B are coefficients with units of 1/°C. F_{opt} is the amplitude of the force exerted by the laser on the membrane. As derived in Methods, we have

$$\dot{T}+CT=k_1+k_2\left(x-x_0\right)^2+k_3\left(x-x_0\right)^4 \tag{8}$$

Now, to obtain the threshold laser power required to generate wave-mixing mediated frequency combs, we neglect the nonlinear term F_{opt} which is associated with the nonlinear harmonics of the phonon lasers. Henceforth, we can write the solution of Eq. (7) as

$$x=a\cos\Omega_0 t+b\sin\Omega_0 t \tag{9}$$

By substituting Eq. (9) in Eq. (8), we get

$$T = T_0 + \sum_{n>0} p_n \cos n\Omega_0 t + \sum_{n>0} q_n \sin n\Omega_0 t \tag{10}$$

We substitute Eq. (9) and Eq. (10) into Eq. (7) and simplify all trigonometric terms in $\Omega_0 t$. By setting the coefficients of $\cos\Omega_0 t$ and $\sin\Omega_0 t$ to zero, we can thus solve for coefficients a and b. Now, we write a and b in terms of the amplitude R and equidistant frequency spacing ω_r of frequency combs as $a = R \cos \omega_r t$ and $b = R \sin \omega_r t$. Henceforth, we derive an expression for the amplitude of frequency combs R as

$$c_1 R^4 + c_2 R^2 + c_3 = 0 \tag{11}$$

where the coefficients c_i are

$$c_1 = C^2 B k_3 + B k_3$$
$$c_2 = 6C^2 B k_3 x_0^2 + 6 B k_3 x_0^2 + 6 C^2 A k_3 x_0 + 24 A k_3 x_0 + C^2 B k_2 + B k_2$$
$$c_3 = 8C^2 A k_3 x_0^3 + 32 A k_3 x_0^3 + 4 C^2 A k_2 x_0 + 16 A k_2 x_0 - 2\gamma C^4 - 10\gamma C^2 - 8\gamma$$

An expression can also be obtained for the equidistant frequency spacing of the frequency comb ω_r. By phenomenology, we know that $\omega_r \propto k_1, k_2, k_3 \propto g_{\text{opt}} \propto \Delta\theta$ and also R is independent of $\Delta\theta$. This is true if the damping coefficient $\gamma \to 0$. Equation (11) can be solved for P:

$$P = \frac{3\gamma\left(C^2+1\right)\left(C^2+4\right)}{2\pi^2 D \xi K} \tag{12}$$

where

$$K = \lambda_1 R^4 + \lambda_2 R^2 + \lambda_3$$
$$\lambda_1 = -4\pi^2 B\left(C^2+1\right)$$
$$\lambda_2 = -24\pi^2 B\left(C^2+1\right)x_0^2 - 24\pi^2 A\left(C^2+4\right)x_0 + 3B\left(C^2+1\right)$$
$$\lambda_3 = -4A\left(C^2+4\right)x_0\left(8\pi^2 x_0^2 - 3\right)$$

Equation (12) thus provides an expression for the laser power P that is required to generate frequency combs with an amplitude of R.

Reference

[S1] de Jong, M. H. J., Ganesan, A., Cupertino, A., Groblacher, S. & Norte, R. A. Mechanical overtone frequency combs. *Nat. Commun.* **14**, 1458 (2023).

[S2] Mahboob, I., Wilmart, Q., Nishiguchi, K., Fujiwara, A. & Yamaguchi, H. Tuneable electromechanical comb generation. *Appl. Phys. Lett.* **100**, 113109 (2012).

[S3] Seitner, M. J., Abdi, M., Ridolfo, A., Hartmann, M. J. & Weig, E. M. Parametric oscillation, frequency mixing, and injection locking of strongly coupled nanomechanical resonator modes. *Phys. Rev. Lett.* **118**, 254301 (2017).

[S4] Ganesan, A., Do, C. & Seshia, A. Frequency transitions in phononic four-wave mixing. *Appl. Phys. Lett.* **111**, 064101 (2017).

[S5] Mahboob, I., Dupuy, R., Nishiguchi, K., Fujiwara, A. & Yamaguchi, H. Hopf and period-doubling bifurcations in an electromechanical resonator. *Appl. Phys. Lett.* **109**, 073101 (2016).

[S6] Goryachev, M., Galliou, S. & Tobar, M. E. Generation of ultralow power phononic combs. *Phys. Rev. Res.* **2**, 023035 (2020).

[S7] Chiout, A. et al. Multi-order phononic frequency comb generation within a MoS_2 electromechanical resonator. *Appl. Phys. Lett.* **119**, 173102 (2021).

[S8] Keskekler, A., Arjmandi-Tash, H., Steeneken, P. G. & Alijani, F. Symmetry-breaking-induced frequency combs in graphene resonators. *Nano Lett.* **22**, 6048–6054 (2022).

[S9] Kuang, T. et al. Optical confinement efficiency in the single beam intracavity optical tweezers. *Opt. Express* **28**(24), 35734–35747 (2020).

[S10] Davidovikj, D. et al. Nonlinear dynamic characterization of two-dimensional materials. *Nat. Commun*. **8**, 1253 (2017).

[S11] Metzger, C., Karrai, K. Cavity cooling of a microlever. *Nature* **432**, 1002–1005 (2004).